Theoretical and numerical investigation of diffusive instabilities in multi-component alloys

Arka Lahiri[a,*], Abhik Choudhury[a]

[a] *Department of Materials Engineering, Indian Institute of Science, Bangalore - 560 012, India.*

arXiv:1607.02570v1 [cond-mat.mtrl-sci] 9 Jul 2016

Abstract

Mechanical properties of engineering alloys are strongly correlated to their microstructural length scale. Diffusive instabilities of the Mullins-Sekerka type is one of the principal mechanisms through which the scale of the microstructural features are determined during solidification. In contrast to binary systems, in multicomponent alloys with arbitrary interdiffusivities, the growth rate as well as the maximally growing wavelengths characterizing these instabilities depend on the the dynamically selected equilibrium tie-lines and the steady state growth velocity. In this study, we derive analytical expressions to characterize the dispersion behavior in isothermally solidified multicomponent (quaternary) alloys for different choices of the inter-diffusivity matrices and confirm our calculations using phase-field simulations. Thereafter, we perform controlled studies to capture and isolate the dependence of instability length scales on solute diffusivities and steady state planar front velocities, which leads to an understanding of the process of length scale selection during the onset of instability for any alloy composition with arbitrary diffusivities, comprising of both independent and coupled diffusion of solutes.

Keywords: Phase-field, Mullins-Sekerka, multi-component, quaternary, diffusion

1. Introduction

Morphological instability of a solid-liquid interface to small perturbations is the basis for the most commonly observed solidification microstructure of dendrites. Experimentally, a planar solidification front during solidification is usually perturbed, either by random thermal fluctuations or due to interactions with insoluble impurities [1]. An unstable solidification front is characterized by amplification of such interfacial perturbations which ultimately develop into cellular or dendritic structures. Any random infinitesimal perturbation can be thought of as a linear combination of a multitude of wavelengths with different amplitudes (which are small during early stages). Thus, the stability of a solid-liquid interface to the amplification of these perturbations can be understood by investigating the growth behavior of the individual modes. Mullins and Sekerka in their classical work [2] present a linear stability analysis of an interface perturbed by any generic wavelength and provide expressions for their growth rates for a binary alloy. This allows the determination of the maximally (fastest) growing wavelength, that principally can be related to the length scales in the cellular or dendritic microstructures. Cells and dendrites, being the most commonly observed solidification structures, have been investigated theoretically [3, 4, 5, 6, 7, 8, 9, 10], experimentally [11, 12, 13, 14, 15, 16, 17, 18], and as well as through simulations [19, 20, 21, 22, 23, 24].

The theory in [2] (also confirmed by phase-field sim-

*Corresponding author

Email addresses: arka@platinum.materials.iisc.ernet.in (Arka Lahiri), abhiknc@materials.iisc.ernet.in (Abhik Choudhury)

ulations in [25]), reveals that the instability length scale in a binary alloy is a function of the equilibrium compositions in the solid and the liquid, the composition of the supersaturated liquid (or equivalently the growth velocity in directionally solidified systems) and the solute diffusivities.

For multicomponent alloys, the equilibrium compositions of the phases (or the effective tie-line) is a function of the inter-diffusivity matrix. This selection of equilibrium tie-lines during growth introduces an additional degree of freedom which influences the behavior of the perturbations and thereby the length scales. This phenomenon of selection of tie-lines during growth of a planar interface has not been addressed by the theoretical discussions of morphological instability in directionally solidified multicomponent systems till now. Among the earliest in this regard is the study performed by Coates et al. [26], which is carried out in the context of a ternary alloy with no diffusional interaction amongst solutes, with the dispersion behavior (the amplification rates for different wavelengths of perturbations) calculated assuming a steady state behavior in the perturbed state. The correctness of this assumption is investigated by Coriell et al. [27] by solving for the time dependent problem which lead to the validation of the steady-state assumption in [26]. The effect of coupled solute diffusivities on the stability of the system to infinitesimal perturbations is studied by Hunziker [28], but without accounting for the possibility of a shift in the tie-lines playing a role in the selection of instability length scales.

The fact that the diffusivity matrix in a multicomponent system influences the dynamic selection of tie-lines and growth velocities, has a considerable impact on the instability behavior. Furthermore, in the context of the difficulties associated with experimental determination of diffusivities in multicomponent alloy systems, a theoretical or a numerical understanding of the instability behavior as a function of solute diffusivities becomes even more important. This motivates our study where we isolate the effect of each of these factors: diffusivity, steady-state (solidification by advancement of a planar front) growth velocity and tie-line compositions, to explain the problem of microstructural length scale selection in multicomponent systems displaying either independent or coupled diffusion of solutes. In this paper, we derive an analytical theory and perform phase field simulations to establish all our major conclusions, with the context being that of an isothermally solidifying system in contrast to the directional solidification studies mentioned in the preceding paragraphs. We start with the theoretical analysis of the growth of perturbations and thereafter describe the phase-field model, followed by the results.

2. Theory

We begin with steady-state (planar front solidification) of a K component alloy. The $K-1$ independent components have no diffusional interaction (i.e., the diffusivity matrix is diagonal) in the liquid, while there is no diffusion in the solid. The governing equation in a frame attached to the interface growing at a velocity V [1] is,

$$D_{ii}\frac{\partial^2 c_i}{\partial z^2} + V\frac{\partial c_i}{\partial z} = 0, \tag{1}$$

where c_i denotes the concentration and D_{ii} the diffusivity of the i'th component in the liquid, with $i = 1, 2, 3, \ldots, K-1$. z is the direction normal to the solid-liquid interface (located at $z = 0$). Consideration of uncoupled diffusion of solutes, enables us to present the following discussion in terms of a generic component i, which stands for all the components in a system.

The solution to Eq. 1 has to obey the following boundary conditions:

$$c_i = c_{i,eq}^{l}, \text{ at } z = 0, \tag{2}$$

[1] the value which is asymptotically approached, late into the scaling regime.

which is the equilibrium composition in the liquid given by the tie-line selected during growth, and,

$$Vc^l_{i,eq}(1-k_i) = -D_{ii}\frac{\partial c_i}{\partial z}\bigg|_{z=0} = -D_{ii}G_i, \qquad (3)$$

which is the Stefan boundary condition at a solid-liquid interface moving with velocity V. G_i is the gradient in c_i at the planar interface. k_i is the equilibrium partition coefficient corresponding to the selected tie-line. The solution to Eq. 1 which conforms to the boundary conditions in Eqs. 2 and 3, is given by,

$$c_i = c^l_{i,eq} + \frac{G_i D_{ii}}{V}\left[1 - \exp\left(\frac{-Vz}{D_{ii}}\right)\right]. \qquad (4)$$

The steady-state solidification described above is now modified by introducing a sinusoidal perturbation given by,

$$z = \Phi = \delta(t)\sin\omega x, \qquad (5)$$

with x being one of the directions parallel to the unperturbed interface (normal to z). Despite δ being a function of time (t), a stability criterion derivable from the steady state solution will not differ appreciably from that obtained by solving the time dependent problem [26, 27], which leads to the following governing differential equation describing a system with interfacial perturbations,

$$D_{ii}\frac{\partial^2 \widetilde{c_i}}{\partial z^2} + D_{ii}\frac{\partial^2 \widetilde{c_i}}{\partial x^2} + V\frac{\partial \widetilde{c_i}}{\partial z} = 0, \qquad (6)$$

where the modified composition field of any generic component i, under interfacial perturbation is denoted by $\widetilde{c_i}$. The form of the solution to Eq. 6, is obtained by adding a term to the steady-state solution given by Eq. 4, which represents a sinusoidal variation in the composition fields in response to the interfacial perturbation of a similar character. It must be taken into account that such an effect diminishes in magnitude with distance from the interface, leading to the following expression,

$$\begin{aligned}\widetilde{c_i} &= c_i + E_i \sin\omega x \exp\left(-k^{(i)}_\omega z\right) \\ &= c^l_{i,eq} + \frac{G_i D_{ii}}{V}\left[1 - \exp\left(\frac{-Vz}{D_{ii}}\right)\right] \\ &\quad + E_i \sin\omega x \exp\left(-k^{(i)}_\omega z\right), \end{aligned} \qquad (7)$$

where $k^{(i)}_\omega$ and E_i are constants. The constant $k^{(i)}_\omega$ is determined by the requirement that the composition profile given by Eq. 7 satisfies the governing Eq. 6, resulting in a quadratic equation in $k^{(i)}_\omega$, which yields,

$$k^{(i)}_\omega = \frac{V}{2D_{ii}} + \sqrt{\left(\frac{V}{2D_{ii}}\right)^2 + \omega^2}. \qquad (8)$$

The compositions in the liquid at the perturbed interface are no longer given by the equilibrium tie-lines selected during steady-state growth because of the Gibbs-Thomson correction. The composition deviations conform to the interfacial curvature, which is approximated by the second derivative of z with respect to x from Eq. 5 and can be seen to be of the same form as the perturbation itself. Thus, the composition in the liquid at the perturbed interface is given by,

$$c_{i,\Phi} = c^l_{i,eq} + b_i\delta\sin\omega x, \qquad (9)$$

where b_i is a constant. Evaluating the solution to the perturbed problem given by Eq. 7 at the perturbed interface (see Eq. 5), we retrieve,

$$c_{i,\Phi} = c^l_{i,eq} + (G_i\delta + E_i)\sin\omega x - \delta k^{(i)}_\omega E_i \sin^2\omega x. \qquad (10)$$

Separately comparing the Fourier coefficients and the leading order constant from Eq. 9 and Eq. 10, we derive,

$$E_i = \delta(b_i - G_i). \qquad (11)$$

Eq. 11 is only a reformulation of E_i in terms of b_i, which is still unknown. The b_i's (b_1, b_2, $\cdots$, b_{k-1}) are related to each other through the fact that each of the composition fields ($\widetilde{c_i}$) satisfies the Stefan condition at the perturbed interface, moving at a velocity ($v(x)$). This implies that the same amplification factor ($\dot{\delta}/\delta$) must be obtained by considering the diffusion field of any one of the components.

The expression for the Stefan condition at the perturbed interface, is given by,

$$v(x) = \left(V + \dot{\delta}\sin\omega x\right) c_{i,\Phi}\left(1 - k_i\right) = -D_{ii}\frac{\partial \widetilde{c_i}}{\partial z}\bigg|_{z=\delta\sin\omega x}, \quad (12)$$

where $\dot{\delta}$ is $d\delta/dt$. The above equation can be re-expressed as:

$$\left(V + \dot{\delta}\sin\omega x\right) = \frac{-D_{ii}}{c_{i,\Phi}\left(1-k_i\right)}\frac{\partial \widetilde{c_i}}{\partial z}\bigg|_{z=\delta\sin\omega x}. \quad (13)$$

From Eq. 9,

$$\frac{1}{c_{i,\Phi}} = \frac{1}{c^l_{i,eq}\left(1 + \frac{b_i}{c^l_{i,eq}}\delta\sin\omega x\right)} \approx \frac{1}{c^l_{i,eq}}\left(1 - \frac{b_i}{c^l_{i,eq}}\delta\sin\omega x\right), \quad (14)$$

where, we have limited ourselves to terms linear in δ. Employing Eq. 11 in the expression obtained by differentiating Eq. 7 with respect to z, we derive,

$$\begin{aligned}\frac{\partial \widetilde{c_i}}{\partial z}\bigg|_{z=\delta\sin\omega x} &= G_i\left(1 - \frac{V\delta\sin\omega x}{D_{ii}}\right) \\ &\quad - k_\omega^{(i)}E_i\sin\omega x(1 - k_\omega^{(i)}\delta\sin\omega x) \\ &\approx G_i - \left(\frac{G_iV}{D_{ii}} + k_\omega^{(i)}(b_i - G_i)\right)\delta\sin\omega x,\end{aligned} \quad (15)$$

by limiting ourselves to terms linear in δ. Equating the Fourier coefficients from both sides of Eq. 13, we get:

$$\frac{\dot{\delta}}{\delta} = V\widetilde{\omega_i}\left[-\frac{b_i}{G_i} + \frac{1}{\widetilde{\omega_i}}\left(k_\omega^{(i)} - \frac{V}{D_{ii}}\right)\right], \quad (16)$$

where,

$$\widetilde{\omega_i} = k_\omega^{(i)} - \frac{V}{D_{ii}}\left(1 - k_i\right). \quad (17)$$

Invoking the fact that $\dot{\delta}/\delta$ is a quantity unique to the system as a whole, regardless of the choice of component (i.e., i) in Eq. 16, leads to $K-2$ relations inter-relating the b_i's $(b_1, b_2, \cdots b_{k-1})$. To express all b_i's $(i \neq 1)$ in terms of b_1, we equate the algebraic expressions for $\dot{\delta}/\delta$ corresponding to each component, which writes as:

$$V\widetilde{\omega_i}\left[-\frac{b_i}{G_i} + \frac{1}{\widetilde{\omega_i}}\left(k_\omega^{(i)} - \frac{V}{D_{ii}}\right)\right] = V\widetilde{\omega_1}\left[-\frac{b_1}{G_1} + \frac{1}{\widetilde{\omega_1}}\left(k_\omega^{(1)} - \frac{V}{D_{11}}\right)\right], \quad (18)$$

which leads to,

$$b_i = \frac{G_i}{\widetilde{\omega_i}}\left[\frac{b_1}{G_1}\widetilde{\omega_1} + \left(k_\omega^{(i)} - \frac{V}{D_{ii}}\right) - \left(k_\omega^{(1)} - \frac{V}{D_{11}}\right)\right]. \quad (19)$$

Now, using Eq. 19, the question of determining b_i corresponding to all the $K-1$ components is reduced to the problem of determining b_1 only. This is achieved by imposing local equilibrium conditions at the perturbed interface, which manifests as compositions of the solid and liquid phases calculated from the Gibbs-Thomson condition (refer to the Appendix for details).

3. Phase-field model

The diffuse interface model used to study the current problem of interest is described in [29]. The grand-canonical density functional (Ω) of the system is given by:

$$\Omega\left(\boldsymbol{\mu}, T, \phi\right) = \int_V \left[\Psi\left(\boldsymbol{\mu}, T, \phi\right) + \left(\epsilon\sigma|\nabla\phi|^2 + \frac{1}{\epsilon}w\left(\phi\right)\right)\right] dV. \quad (20)$$

The values of the order parameter (ϕ, also known as the phase-field) demarcates regions of pure solid ($\phi = 1$), pure liquid ($\phi = 0$) and the interface between the two (where ϕ is a positive fraction), in the solidification microstructure. The double-welled polynomial $w(\phi) = 9\sigma\phi^2\left(1-\phi\right)^2$, introduces a potential barrier between the solid and the liquid phases. A penalty in grand potential associated with the gradients in ϕ is introduced into the model through the term $\sigma|\nabla\phi|^2$. ϵ controls the interface width and σ denotes the interfacial energy respectively. The grand potential density Ψ of the system is obtained by an interpolation of the grand potentials of the solid and the liquid phases,

$$\Psi\left(\boldsymbol{\mu}, T, \phi\right) = \Psi^l\left(\boldsymbol{\mu}, T\right)h\left(1-\phi\right) + \Psi^s\left(\boldsymbol{\mu}, T\right)h\left(\phi\right), \quad (21)$$

where Ψ^s and Ψ^l are functions of the diffusion potential vector $\boldsymbol{\mu} = \{\mu_1, \ldots, \mu_{K-1}\}$ (assuming a substitutional alloy under lattice constraint with K components) and the temperature (T) in the system. $h\left(\phi\right) = \phi^2\left(3 - 2\phi\right)$

is an interpolation polynomial with the property $h(\phi) + h(1-\phi) = 1$.

The compositions in every phase can be derived as functions of the diffusion potential vector $\boldsymbol{\mu}$ as given by:

$$c_i^{s,l}(\boldsymbol{\mu}, T) = -V_m \frac{\partial \Psi^{s,l}(\boldsymbol{\mu}, T)}{\partial \mu_i}. \tag{22}$$

The molar V_m is taken to be a constant across all the components.

Solidification (or melting) is captured by the evolution of ϕ, which is obtained by solving:

$$\tau_{sl}\epsilon \frac{\partial \phi}{\partial t} = 2\sigma\epsilon\nabla^2\phi - \frac{1}{\epsilon}\frac{\partial w(\phi)}{\partial \phi} - \frac{\partial \Psi(\boldsymbol{\mu}, T, \phi)}{\partial \phi}. \tag{23}$$

τ_{sl} is the relaxation time with its value set to obtain a diffusion controlled interface motion [30].

For solidification in a multi-component system, the evolution of $\boldsymbol{\mu}$ can be expressed as:

$$\left\{\frac{\partial \mu_i}{\partial t}\right\} = \left[\sum^{p=s,l} h_p(\phi) \frac{\partial c_i^p(\boldsymbol{\mu}, T)}{\partial \mu_j}\right]^{-1}_{ij} \Big\{\nabla \cdot \sum_{j=1}^{K-1} M_{ij}(\phi) \nabla \mu_j - \sum^{p=s,l} c_i^p(\boldsymbol{\mu}, T) \frac{\partial h_p(\phi)}{\partial t}\Big\}. \tag{24}$$

where $[\,\cdot\,]$ denotes a matrix of dimension $((K-1)\times(K-1))$ while $\{\,\cdot\,\}$ represents a vector of dimension $(K-1)$, and we have used $h_l(\phi) = h(1-\phi)$ and $h_s(\phi) = h(\phi)$. The atomic mobility, $M_{ij}(\phi)$ is obtained by interpolating the individual phase mobilities,

$$M_{ij}(\phi) = M_{ij}^l(1-\phi) + M_{ij}^s\phi, \tag{25}$$

where, each of the mobility matrix $M_{ij}^{s,l}$ is defined by,

$$\left[M_{ij}^{s,l}\right] = \left[D_{ik}^{s,l}\right]\left[\frac{\partial c_k^{s,l}(\boldsymbol{\mu}, T)}{\partial \mu_j}\right], \tag{26}$$

where $D_{ij}^{s,l}$ are the solute inter-diffusivities.

In our calculations, the solute diffusivities are assumed to be negligibly small in the solid compared to the liquid. This assumption leads to an anomalous solute trapping that is corrected by using an anti-trapping current [30].

4. Thermodynamics

The thermodynamic input for the phase-field model comprises of the equilibrium compositions of the phases, the inverse of the matrix $\left[\frac{\partial \mu_i}{\partial c_j}\right]$ which is computed at the equilibrium compositions of the phases. For computing the matrix $\left[\frac{\partial \mu_i}{\partial c_j}\right]$, in the present work we use an ideal solution approximation for representing the free energies, described in detail in the Appendix. Thereafter, we perform a linearization of the phase-diagram (mentioned in the Appendix) using the aforementioned properties giving us the relation between the compositions and the chemical potentials as,

$$\left\{c_i^{l,s}\right\} = \left\{c_{i,eq}^{l,s,*}\right\} + \left[\frac{\partial c_i^{l,s}}{\partial \mu_j}\right]\left\{\mu_j - \mu_{j,eq}^*\right\}, \tag{27}$$

for all the $K-1$ independent components while $\mu_{j,eq}^*$ are the values of the equilibrium diffusion potentials of the components computed at the equilibrium compositions $\left(c_{i,eq}^{l,s,*}\right)$, about which the properties are linearized.

The driving force for phase transformation $(\Delta\Psi^{ls}(\boldsymbol{\mu}, T))$ which is also required for the phase-field computations is due to the difference in grand potentials of the participating phases $\Psi^l(\boldsymbol{\mu}, T)$ and $\Psi^s(\boldsymbol{\mu}, T)$ which at leading order in $\boldsymbol{\mu}$ reads,

$$\Delta\Psi^{ls} = \frac{1}{V_m}\left\{c_{i,eq}^{s,*} - c_{i,eq}^{l,*}\right\}\left\{\mu_i - \mu_{i,eq}^*\right\}. \tag{28}$$

5. Results

In our bid to understand the behavior of $\dot{\delta}/\delta$ as a function of ω $(= 2\pi/\lambda)$, as predicted by Eq. 16 and the phase-field simulations, a Hf-Re-Al-Ni quaternary alloy was selected as the system of study. The equilibrium tie-line compositions obtained from the Thermotech Ni- based Superalloys Database (TTNI8) available with the Thermo-Calc software and the methodology adopted for obtaining the relevant thermodynamic information is mentioned in the Appendix. While discussing our key observations, we

will adhere to the generic representation of solutes by A, B and C, with D denoting the solvent in order to remain consistent with our theoretical expressions and discussion of the phase field modelling technique. Thus, for all practical purposes in the discussion that follows, A, B, C and D stand for Hf, Re, Al and Ni respectively.

Henceforth, most of our discussion will revolve around the behavior of the salient features of a dispersion plot: the maximum in $\dot{\delta}/\delta$ ($(\dot{\delta}/\delta)_{max}$), the wave number corresponding to the maximum in $\dot{\delta}/\delta$ (ω_{max}), and the wave number at which $\dot{\delta}/\delta$ changes sign (ω_{crit}), as functions of different parameters. The significance of ω_{max} can be understood as the parameter which defines the dominating length scale ($\lambda_{max} = 2\pi/\omega_{max}$) characterizing the early stages of instability, whereas, ω_{crit} defines a length scale ($\lambda_{crit} = 2\pi/\omega_{crit}$) below which the solid-liquid interfacial energy dominates, causing extremely small solidified features to melt back. $(\dot{\delta}/\delta)_{max}$ is the term characterizing the magnitude of the fastest growing mode. It sets the time scale of the Mullins-Sekerka instability; larger values of which imply a quicker destabilization to a cellular or dendritic microstructure.

At the onset, the principal aim of the simulations and the analytical studies is to derive the sensitivity of the alloy system towards the amplification of the instabilities for different choices of the inter-diffusivities of the elements. Scientifically, this is an important question, as these are difficult quantities to determine experimentally. Secondly, the comparison between the analytical calculations and the phase-field simulations also benchmarks the model for use in solidification simulations in multicomponent alloys. Therefore, in this sub-section, we will derive the dispersion relations using both phase-field simulations and analytical calculations for a "given alloy composition" while we vary the inter-diffusivity matrices.

For setting up the phase-field simulations for comparison to the analytical calculations, it is essential to initialize the system very close to the assumptions that are inherent in the analysis. Therefore, we start from the phase-field simulation of a planar growth front in a supersaturated liquid and let the chemical potential and phase-field profiles develop well into the scaling regime (where the square of the interface position x_f^2 scales linearly with time with a defined constant of proportionality η_s). Here, the variation of the velocity occurs over time-scales which are much larger than that required for the interface to traverse a distance corresponding to several times the interfacial width. The equilibria along with the planar front velocity (V) recorded from the plane front solidification simulation, were utilized to compute the composition gradients of different components at the interface (G_i), all of which appeared in the theoretical calculation of the dispersion curve. This ensured a uniformity in the parameters used across phase field simulations and analytical calculations.

Thereafter, the 1D composition and phase-field profiles in the liquid are perturbed with prescribed wavelengths defined by the width of the simulation domain possessing an amplitude of 5 grid-points which results in an initialization where the composition and the phase-field profiles suitably conform to the imposed morphological perturbation.

5.1. Comparison between theory and phase-field simulations

We begin our discussion with a comparison of the dispersion plot ($\dot{\delta}/\delta$ versus ω) obtained from phase-field simulation against the one predicted by our analytical theory for a situation with a diagonal diffusivity matrix with $D_{AA} = D_{BB} = D_{CC} = 1.0$ (see Fig. 1). The graph depicts an excellent agreement between the analysis and simulations[2]. It must be mentioned here that all calculations

[2]It must be mentioned at this point that simulations performed for studying the dispersion behavior were restricted to modes with $\omega >= 0.0024$. This was necessitated by an observed tendency of the system to select wavelengths smaller than what the system was initialized with (observed only for small values of ω), as we simulated longer in time.

(both analytical and phase-field) are performed with non-dimensionalized parameters whose values and the relevant scales required to convert them to dimensional values are mentioned in the Appendix.

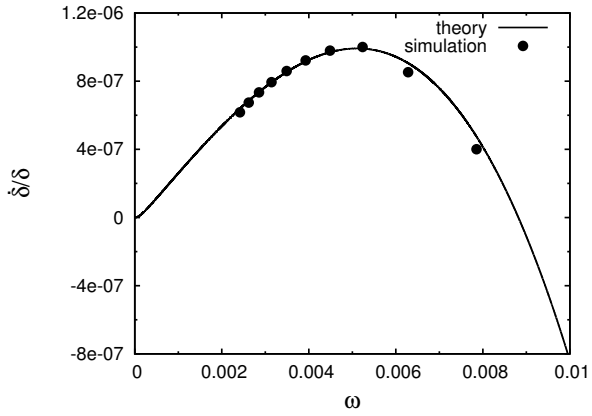

Figure 1: $\dot{\delta}/\delta$ versus ω from phase-field and theoretical calculations. The diffusivity matrix is diagonal with $D_{AA} = D_{BB} = D_{CC} = 1.0$. The bulk liquid composition chosen for this study is: $c_A = 0.001878$, $c_B = 0.0165155$, $c_C = 0.1871735$.

Moving on to situations where the diffusivity matrix is non-identity. In Fig. 2, we present three systems with different combinations of D_{BB} and D_{CC} while D_{AA} was held constant. Here, the analytical curves appear to be more sensitive to a change in D_{BB} than to one in D_{CC}.

With $D_{BB} = 0.8$, the maximally growing wave number (ω_{max}) and the critical wave number (ω_{crit}) move towards left with a slight increase in the magnitude of $(\dot{\delta}/\delta)_{max}$ compared to the cases where $D_{BB} = 0.5$. Thus, it appears that a higher value of D_{BB} leads to the selection of larger length scales of instability. The dispersion plot for $D_{BB} = 0.8$ also appears to have a different shape than the ones with $D_{BB} = 0.5$, which can be discerned by the lower growth rates for wave numbers larger than ω_{max} in the former than in the latter, with the reverse being true for $\omega < \omega_{max}$. This observed change in shape is a natural outcome of the changes in ω_{max}, ω_{crit} and $(\dot{\delta}/\delta)_{max}$ effected by a change in D_{BB}.

In Fig. 3, we study the dispersion relations by maintaining $D_{BB} = 1.0$ for three systems with different combinations of D_{AA} and D_{CC} (lower than D_{BB}). The plots appear to superimpose upholding the observation in Fig. 2 that the dispersion relations are a lot more sensitive to changes in D_{BB} than to modifications in D_{AA} and D_{CC}. Thus, despite variations in D_{AA} and D_{CC}, the instability dynamics and the relevant critical wavelengths remain largely invariant due to constancy of D_{BB}.

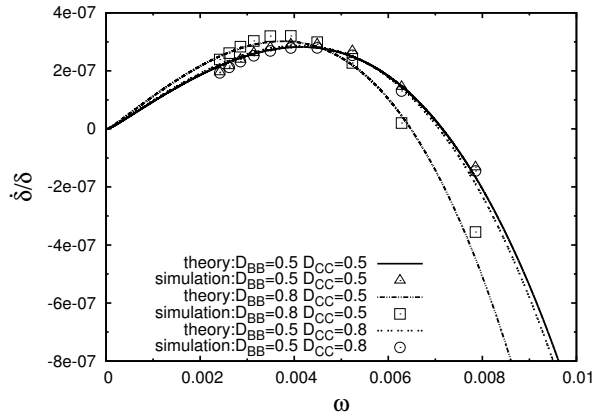

Figure 2: $\dot{\delta}/\delta$ versus ω from phase-field and theoretical calculations. The diffusivity matrix is diagonal with $D_{AA} = 1.0$ with the other diagonal components being mentioned in the figure legend. The bulk liquid composition chosen here is the same as in Fig. 1.

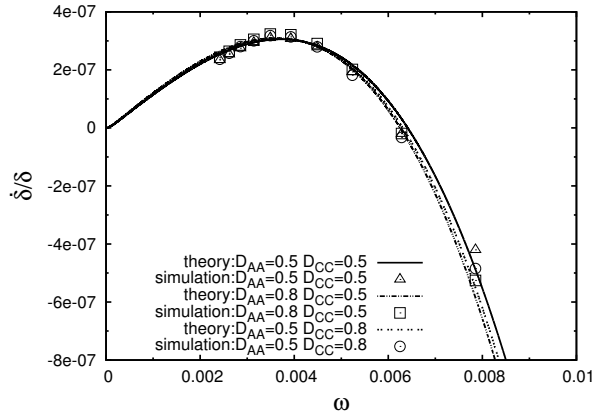

Figure 3: $\dot{\delta}/\delta$ versus ω from phase-field and theoretical calculations. The diffusivity matrix is diagonal with $D_{BB} = 1.0$ with the other diagonal components being mentioned in the figure legend. The bulk liquid composition chosen here is the same as in Fig. 1.

Subsequently, we investigate the situation where we fix $D_{CC} = 1.0$ and vary D_{AA} and D_{BB} (as shown in Fig. 4), for which trends very similar to what observed in Fig. 2,

is retrieved. A higher value of D_{BB} resulted in smaller values for ω_{max} and ω_{crit}, with the wave numbers smaller than ω_{max} growing faster than in systems with a lower value of D_{BB} and vice-versa. Thus, the consequent microstructural implications derivable from Fig. 4, are similar to what was discussed for Fig. 2. Also, as observed in Fig. 2, a higher value in D_{BB} resulted in a higher value for $(\dot{\delta}/\delta)_{max}$.

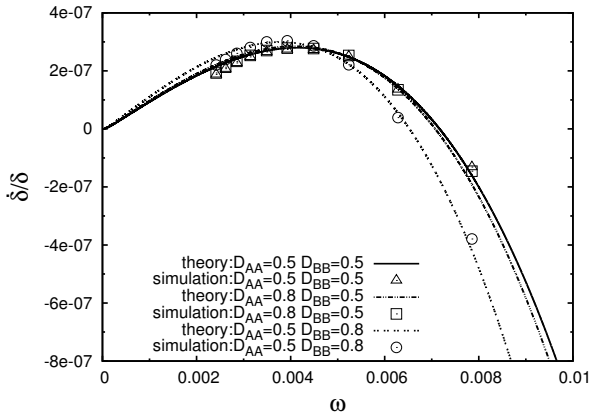

Figure 4: $\dot{\delta}/\delta$ versus ω from phase-field and theoretical calculations. The diffusivity matrix is diagonal with $D_{CC} = 1.0$ with the other diagonal components being mentioned in the figure legend. The bulk liquid composition chosen here is the same as in Fig. 1.

The preceding results established the major trends in the variation of the dispersion relations as functions of diffusivity. It must be reiterated at this point that though the explicit changes were only in the diffusivity matrices, there were also associated changes in the equilibrium tie-line compositions of the planar profiles along with changes in velocity of the interface. So in the studies discussed till now, the inferences we draw upon can be seen as a result of combined changes in the equilibrium compositions at the interface, the velocity and the diffusivities (the equilibrium tie-line compositions and the velocities are enumerated in Table 1.

Thus, to isolate and understand the influence of each of the contributing factors better, we resort to more controlled studies, where we vary only one of the parameters at a time while maintaining the others constant. They are sequentially described in the following subsections.

5.2. Influence of diffusivity

In the first among these, we will investigate the influence of the change in the diffusivity matrices keeping both the velocity as well as the tie-line compositions fixed.In a separate work [31], we study how the equilibrium compositions at the interface can be determined for different choices of diffusivity matrices. Drawing upon this, we isolate alloy compositions giving us the same growth coefficient ($\eta_s = x_f/\sqrt{t}$, x_f being the position of the solid-liquid interface at a time t) for different values of the diffusivity matrices, ensuring at all times that the equilibrium compositions at the interface remain invariant (at the chosen thermodynamic tie-line). For each of these conditions, we can then derive the characteristics of the dispersion behavior which are highlighted by the quantities $(\dot{\delta}/\delta)_{max}$, ω_{max} and ω_{crit} derived using the analytical expressions described in the previous sections, where the velocity V $(= \eta_s/\sqrt{t})$ is computed using an arbitrary time t, which is kept the same for all the diffusivity combinations.

In Fig. 5(a), we report the variation of ω_{max} and ω_{crit} for three different cases, where in each of the situations either of D_{AA}, D_{BB}, D_{CC} is varied while the others are left constant. We see that the ω_{max} (also ω_{crit}) decreases smoothly with increase in diffusivity for all the three cases; the pronounced effect (steeper sensitivity to changes in diffusivity) being for the case where only D_{BB} is varied while D_{AA} and D_{CC} are held constant. The observations are consistent with the fact that as the interdiffusivities of individual components (D_{AA}, D_{BB} or D_{CC}) increases while V and the equilibrium tie-line compositions stay the same, the composition gradients at the planar interface (G_A,G_B and G_C) decreases. This decrease can be qualitatively linked to the weakening of the diffusive instabilities which shifts the critical wavelengths to larger values (or reduction of ω_{max} and ω_{crit}) as highlighted in from Fig. 5(a).

The interesting fact is the difference in the sensitiv-

D_{AA}	D_{BB}	D_{CC}	V	$c^s_{A,eq}$	$c^s_{B,eq}$	$c^s_{C,eq}$	$c^l_{A,eq}$	$c^l_{B,eq}$	$c^l_{C,eq}$
1.0	0.5	0.5	1.07e-04	0.000517	0.023554	0.177660	0.002966	0.009170	0.197032
1.0	0.8	0.5	1.26e-04	0.000539	0.023891	0.178480	0.003092	0.009282	0.197929
1.0	0.5	0.8	1.10e-04	0.000520	0.023404	0.176777	0.002983	0.009112	0.196085
0.5	1.0	0.5	1.28e-04	0.000600	0.024395	0.178584	0.003437	0.009469	0.198042
0.5	1.0	0.8	1.31e-04	0.000606	0.024246	0.177609	0.003467	0.009411	0.196998
0.8	1.0	0.5	1.33e-04	0.000564	0.024154	0.178789	0.003237	0.009377	0.198267
0.5	0.5	1.0	1.06e-04	0.000562	0.023626	0.176222	0.003219	0.009198	0.195484
0.5	0.8	1.0	1.24e-04	0.000592	0.023997	0.176873	0.003392	0.009323	0.196198
0.8	0.5	1.0	1.10e-04	0.000533	0.023421	0.176352	0.003056	0.009121	0.195626

Table 1: Tie-line compositions and steady-state velocities as functions of diffusivities.

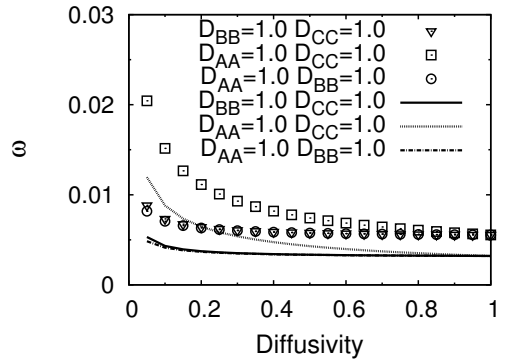

(a)

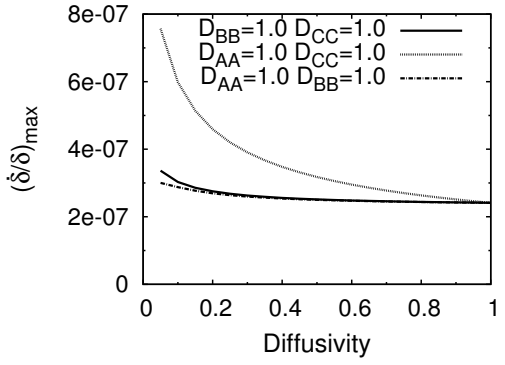

(b)

Figure 5: Plots showing variations of, (a)ω_{max} (shown by lines) and ω_{crit} (shown by points), (b) $(\dot{\delta}/\delta)_{max}$, with change in diffusivity of any one of the components A, B and C (the diffusivity matrix was diagonal). The figure legends reveal the components whose diffusivities are held constant along with the values set for them, while the diffusivity of the component not mentioned in the legend is varied to generate the curve. The value of η_s was selected to be 0.33. The time chosen for analysis was $t = 2000000$.

ities towards change in the inter-diffusivities. For D_{BB} (< 1) the system chooses much larger values for ω_{max} and ω_{crit} as compared to the values chosen for the same magnitudes of D_{AA} and D_{CC}. This behavior can be explained on the basis of the changes in the diffusion length scales (brought about by the change in the diffusivities) and capillary length scales described principally by the Gibbs-Thomson coefficients (and therefore the equilibrium compositions).

In a binary alloy, the changes in the critical length scales, denoted by $(2\pi/\omega_{crit})$ and $(2\pi/\omega_{max})$, approximately scale with $\sqrt{d_o l_D}$, where d_o is the capillary length, and l_D is the diffusion length, each of which can be controlled independently. Thereby, a binary alloy with larger capillary length d_o, will show a higher sensitivity towards changes in l_D with relation to their influence on the critical length scales $(2\pi/\omega_{crit})$ and $(2\pi/\omega_{max})$.

However, in ternary and higher multi-component alloys this correlation becomes difficult to establish as the influence of capillarity (principally related to the term b_i (see Eq. 9)) becomes coupled to the changes in diffusivity (see Eq. 19). Therefore, the material properties which govern the value b_i (which is principally just related to the Gibbs-Thomson coefficient in the case of binary alloys) cannot be explicitly linked to the thermodynamic properties of the

phases $\left[\frac{\partial \mu_i}{\partial c_j}\right]$. In essence, this implies that changes in the capillary lengths and the diffusion lengths become inter-related.

In order to establish this inter-dependence we numerically evaluate the length scales for different equilibrium compositions by changing arbitrarily the composition c_B (which essentially changes the $\left[\frac{\partial \mu_i}{\partial c_j}\right]$ according to Eq. 33 in Appendix) of both phases maintaining the same partitioning between the phases ($\Delta c_{B,eq} = c^l_{B,eq} - c^s_{B,eq}$, remaining constant) and the results are plotted in Fig.6.

We see that with lower compositions of c_B the changes in the critical length scales become more sensitive to the changes of the diffusivity for all three components with the maximum sensitivity being still for the changes in diffusivity of element B.

Further, the consequence of the value of segregation can also be coupled with the above discussion to qualitatively interpret the results displayed in Fig.5. Here, the amount of segregation for the component A is the least while we have similar magnitudes of segregation for the element B and C. So, we can qualitatively conclude, that a smaller phase composition in combination with larger segregation leads to greater sensitivity towards the change in length scales as the diffusivity of that particular component is varied.

The variation in $(\dot{\delta}/\delta)_{max}$ with different component diffusivities show a trend in Fig. 5(b) which can be explained by considering Eq. 16 and the fact that $\widetilde{\omega_B}$ has a magnitude which is much higher than that of $\widetilde{\omega_A}$ and $\widetilde{\omega_C}$ at ω_{max}'s corresponding to respective variations in D_{BB}, D_{AA} and D_{CC}. This in turn is a result of a combination of larger compositional gradients and lower values of compositions (since $\tilde{\omega}_i = k^{(i)}_{\omega} + G_i/c_i$).

5.3. Influence of velocity

Recalling from our work [31] that a multitude of bulk alloy compositions, each corresponding to a different η_s, can grow with the same equilibrium tie-line compositions

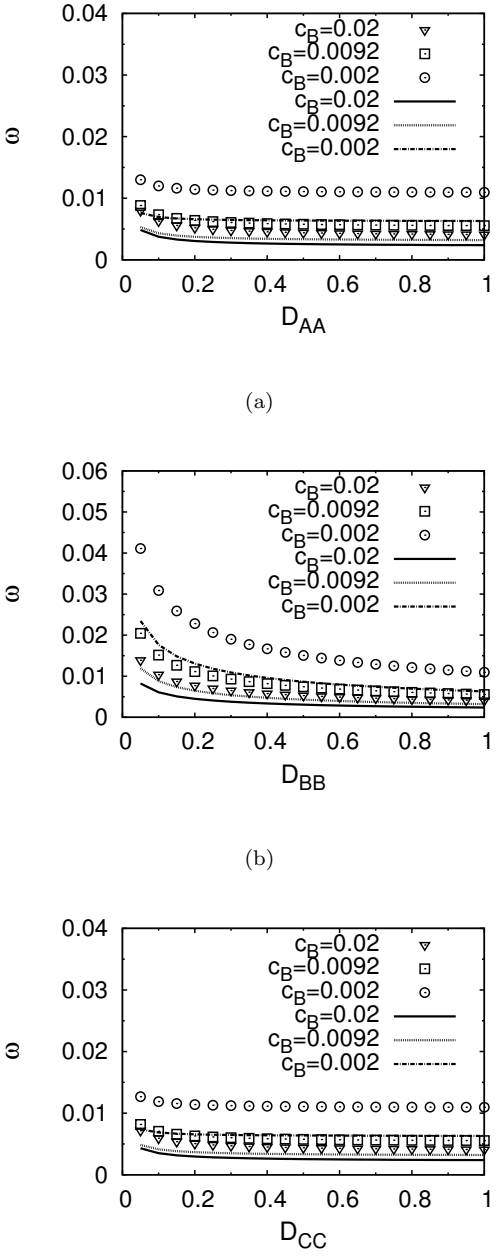

(a)

(b)

(c)

Figure 6: Plots showing variations of ω_{max} (shown by lines) and ω_{crit} (shown by points) with change in diffusivity of the component A in (a), B in (b) and C in (c) each for different values of the composition c_B (the diffusivity of the other two components were held at unity).

(mentioned in the Appendix) for a given diffusivity matrix, allows us to investigate the effects of η_s (which essentially controls the plane front interface velocity, V) on parameters such as ω_{max}, ω_{crit} and $(\dot{\delta}/\delta)_{max}$. We begin our discussion with Figs. 7(a) and 7(b) where ω_{max} and ω_{crit} are plotted against η_s. The general trend of the curves point towards a selection of larger values of ω_{max} and ω_{crit} for higher values of η_s. This is due to the fact that higher planar front velocities (V) associated with higher values of η_s leads to higher magnitudes of composition gradients at the planar interface G_i, which translates to smaller diffusion lengths and consequently the critical and maximally growing wavelengths. The curves corresponding to $D_{BB} = 1.0$ show a much gentler increase with η_s compared to the ones with $D_{BB} = 0.5$, which can be explained based on the discussion accompanying Fig. 5(a). The increase in planar front velocity (V) with η_s is the reason behind the consequent increase in $(\dot{\delta}/\delta)_{max}$ (see Fig. 7(c)), as can be seen from Eq. 16. Furthermore, as discussed earlier, a higher V also leads to a higher G_i, which further increases the value of $(\dot{\delta}/\delta)_{max}$ (see first term in brackets of Eq. 16 (b_i/G_i) which decreases with increase in G_i).

5.4. Influence of alloy compositions on the thermodynamic tie-line

Having individually understood the influence of the velocities and the diffusivities on the Mullins-Sekerka instability, we can now attempt to understand another particular question of engineering importance, which is the prediction of ω_{max}, ω_{crit} and $(\dot{\delta}/\delta)_{max}$ for different alloy compositions along a given thermodynamic tie-line. This study incorporates the changes in the behavior of perturbations owing to the coupled changes in the velocity and the equilibrium tie-lines that are selected. Therefore, this requires a knowledge of the tie-lines that will be selected by the system during planar front growth and the value of η_s characterizing that steady state regime, which can be computed from the expressions mentioned in the Ap-

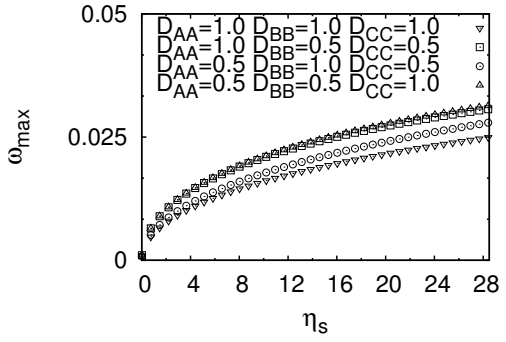

(a)

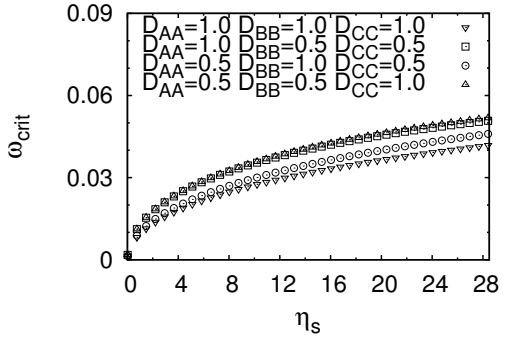

(b)

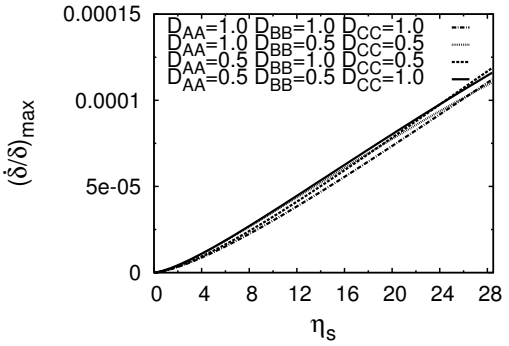

(c)

Figure 7: Plots showing variations of (a)ω_{max}, (b) ω_{crit}, (c) $(\dot{\delta}/\delta)_{max}$, with η_s for different diagonal diffusivity matrices. The time chosen for analysis was $t = 2000000$.

pendix [31]. We perform this study on a series of bulk compositions lying along a pre-selected tie-line (mentioned in the Appendix) resulting in certain interesting trends worth examining.

To this end, we define a parameter ν, which denotes the volume fraction of the solid; a smooth variation in which, allows consideration of different bulk compositions given by: $c^s_{i,eq}\nu + c^l_{i,eq}(1-\nu)$.

From Fig. 8(a), we can see that η_s increases with increasing ν. This is an important information as η_s sets the velocity (V) of the planar interface, which in turn affects the composition gradients at the steady-state interface (G_i) and higher values of both of these parameters have a propensity to make the system more susceptible to growth of perturbations. It must be mentioned here that as we choose different alloy compositions along a given thermodynamic tie-line, the continuous variation in the selection of steady-state growth velocities is accompanied by the system equilibrating at different thermodynamic tie-lines. Thus, different $\Delta c_i = c^l_{i,eq} - c^s_{i,eq}$'s are chosen for different bulk alloy compositions, which also serve to modify the composition gradients at the interface during steady-state growth.

In light of the information presented in Fig. 8(a), we can attempt to understand the increase of ω_{max} and ω_{crit} with η_s as shown in Fig. 8(b). This can be explained by the higher V and G_i's associated with higher values of η_s, which causes the system to choose smaller length scales manifesting as higher values of ω_{max} and ω_{crit}. The reasons for curves corresponding to $D_{BB} = 0.5$ reporting higher values than ones with $D_{BB} = 1$ have already been discussed in conjunction with Fig. 5(a).

From Fig. 8(c) we can find $(\dot{\delta}/\delta)_{max}$ varying against ν in a manner similar to what observed for Fig. 7(c). The increase in η_s with ν as shown in Fig. 8(a), explains the increase in $(\dot{\delta}/\delta)_{max}$ using the arguments associated with Fig. 7(c).

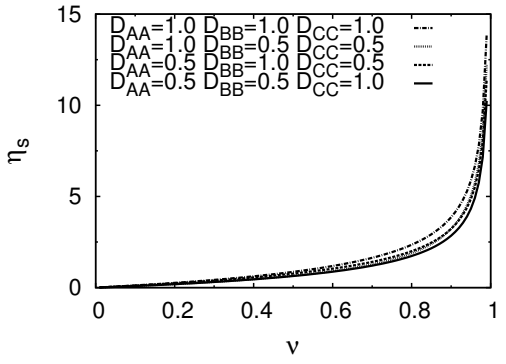

(a)

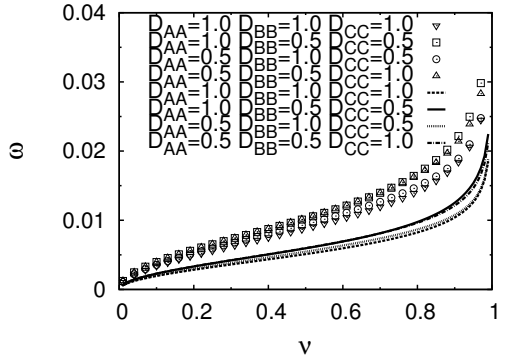

(b)

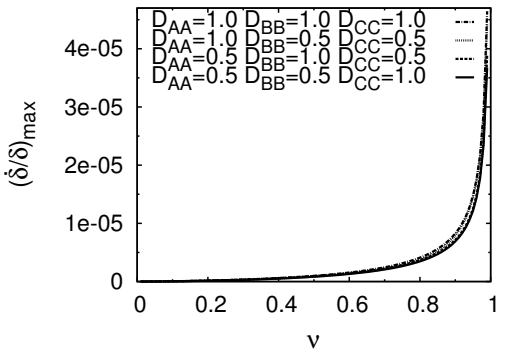

(c)

Figure 8: Plots showing variations of (a)η_s, (b)ω_{max} (shown by lines) and ω_{crit} (shown by points), (c) $(\dot{\delta}/\delta)_{max}$, with ν for different diagonal diffusivity matrices. The time chosen for analysis was $t = 2000000$.

5.5. Influence of off-diagonal terms in the diffusivity matrix

For systems where there is a significant coupling between the diffusion of different solutes, it gives rise to off-diagonal terms in the diffusivity matrix. This introduces complications which preclude most of the analytical techniques we have successfully employed till now. Therefore, we utilize numerical phase-field simulations as a method of studying the Mullins-Sekerka type instabilities, where again we examine the variation of $(\dot{\delta}/\delta)$ with ω. The dispersion behavior for $D_{AB} = D_{BA} = 0.5$ and

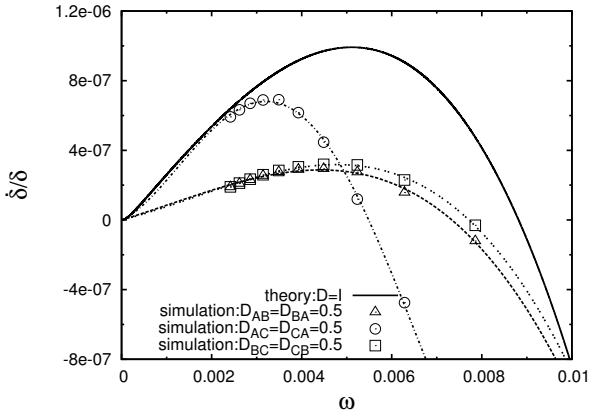

Figure 9: $\dot{\delta}/\delta$ versus ω from phase-field calculations. The figure legend reveals the off-diagonal components which are non-zero with all the diagonal components set to 1. The continuous line represents the analytical dispersion plot for $D = I$ and the discontinuous lines are polynomial functions (cubic for $D_{AB} = 0.5$ and $D_{BC} = 0.5$; quartic for $D_{AC} = 0.5$) fitted to the simulation data points. The bulk liquid composition chosen here is the same as in Fig. 1.

$D_{BC} = D_{CB} = 0.5$ are similar, with both reporting values of $(\dot{\delta}/\delta)$ an order of magnitude lower than that for $D = I$ with the ω_{max} (around 0.0044 for both $D_{AB} = 0.5$ and $D_{BC} = 0.5$) taking up values similar to the case for $D = I$ ($\omega_{max} = 0.0051$). The case corresponding to $D_{AC} = D_{CA} = 0.5$ produces a behavior much different to what is observed for the other combinations. Here, for wavenumbers smaller than ω_{max} ($= 0.0032$) the values for $(\dot{\delta}/\delta)$ are very similar to the ones corresponding to $D = I$ but it drops sharply for wavenumbers larger than ω_{max} resulting in a plot whose ω_{crit} almost coincides with the ω_{max} for $D = I$.

6. Summary & Conclusions

Solidification of a multicomponent alloy with unequal solute diffusivities is associated with a shift of the interfacial compositions from the originally selected thermodynamic tie-line on which the alloy composition is located. These characteristics of the transformation influence the growth behavior of morphological perturbations and thereby influence the selection of microstructural length scales.

In this study, we attempt to isolate and understand the effect of each of the parameters (i.e., diffusivities, steady-state growth velocities and tie-line compositions) on the dispersion behavior of a multicomponent alloy. Here, we develop an analytical theory (and benchmark it against phase field simulations) and employ it to study the instabilities in a Hf-Re-Al-Ni quaternary system (A, B, C and D stand for Hf, Re, Al and Ni respectively).

From our analytical calculations, it is observed that increase in diffusivity (the equilibrium tie-line and the growth velocity being kept constant) of any one of the components leads to a selection of larger length scales (lower ω_{max} and ω_{crit}) during the onset of instability consistent with the lower composition gradients at the interface.

The instability length scales $(2\pi/\omega_{max})$, and $(2\pi/\omega_{crit})$, are seen to reduce with an increase in V (for a given diffusivity matrix and equilibrium compositions of the phases), which is explained by taking into account the combined influence of V and the resultant planar composition gradients (G_i)'s.

Having understood the changes affected by varying diffusivity and the steady state velocity, we focus on a problem of engineering interest where the prediction of the dispersion behavior of an arbitrary alloy with known diffusivities is sought. A series of bulk alloy compositions along a selected thermodynamic tie-line choose different equilibrium compositions and growth velocities during steady-

state growth, which can be correlated to the observed trends in instability length scales on the basis of the concepts developed in the previous studies.

An analytical theory similar to the one for off-diagonal diffusivities is mathematically complex. Hence, to study the influence of the presence of cross diffusion terms in the diffusivity matrix on the dispersion behavior, we employ phase field simulations, which reveal the effect of a non-zero D_{AC} on the instability length scales to be significantly different from that obtained with non-zero terms of D_{BC} or D_{AB}, for the chosen system thermodynamics.

To conclude, we have been able to identify and understand the factors determining the length scale selection in microstructures arising out of Mullins-Sekerka type instabilities in multicomponent alloys. We have shown that our analytical expressions (for independent diffusion of solutes) and phase field simulations (for both independent and coupled diffusion of solutes) are equally capable of predicting the instability dynamics and length scales during solidification. This has important implications in casting of engineering alloys as it allows an efficient control on the microstructural length scales.

7. Acknowledgments

We are grateful to Prof. Dipankar Banerjee and K. S. Vinay, of the Department of Materials Engineering, Indian Institute of Science, for bringing this particular problem to our notice and helping us with the retrieval of the relevant thermodynamic information from Thermo-Calc. We also thank Sebastian Schulz, of the Institute of Materials and Processes, Karlsruhe University of Applied Sciences, who is working on a similar problem for ternary systems, for critical and insightful discussions.

8. Appendix

8.1. Equilibrium across a curved interface

For determining b_i Eq. 28 can be restated as,

$$\frac{1}{V_m}\sum_{i=1}^{K-1}\sum_{j=1}^{K-1}\frac{\partial\mu_i}{\partial c_j}(c_{j,\Phi}-c^l_{j,eq})(c^s_{i,eq}-c^l_{i,eq}) = \frac{1}{V_m}\sum_{i=1}^{K-1}\sum_{j=1}^{K-1}\frac{\partial\mu_i}{\partial c_j}(b_j\delta\sin\omega x)(c^s_{i,eq}-c^l_{i,eq}) = \sigma\kappa = \sigma\delta\omega^2\sin\omega x, \tag{29}$$

where we have used Eq. 9 to obtain the second equality.

8.2. Linearized phase diagram

The coexistence surfaces are defined by the inter-relationships between $\mu_{i,eq}$, given by,

$$\Delta\Psi^{ls} = \frac{1}{V_m}\left\{c^{s,*}_{i,eq}-c^{l,*}_{i,eq}\right\}\left\{\mu_{i,eq}-\mu^*_{i,eq}\right\} = 0. \tag{30}$$

This leads to phase compositions along the equilibrium coexistence surfaces, computed as,

$$\left\{c^{l,s}_{i,eq}\right\} = \left\{c^{l,s,*}_{i,eq}\right\} + \left[\frac{\partial c^{l,s}_i}{\partial\mu_j}\right]\left\{\mu_{j,eq}-\mu^*_{j,eq}\right\}. \tag{31}$$

8.3. Equilibrium compositions and thermodynamic parameters

The equilibrium compositions chosen for the liquid: $c^l_A = 0.0032$, $c^l_B = 0.0092$, and $c^l_C = 0.1969$, and that for the solid (γ): $c^s_A = 0.000556$, $c^s_B = 0.023831$, $c^s_C = 0.177447$. The data corresponds to a temperature of 1689K.

The $\partial c/\partial\mu$ matrices were derived by assuming a free energy density of the form:

$$f = \sum_i c_i \ln c_i, \tag{32}$$

which corresponds to a dilute limit approximation. Assuming, D to be the solvent we compute $\partial\mu/\partial c = \partial^2 f/\partial c^2$ as:

$$\frac{\partial\mu}{\partial c} = \begin{bmatrix} \frac{1}{c_A}+\frac{1}{c_D} & \frac{1}{c_D} & \frac{1}{c_D} \\ \frac{1}{c_D} & \frac{1}{c_B}+\frac{1}{c_D} & \frac{1}{c_D} \\ \frac{1}{c_D} & \frac{1}{c_D} & \frac{1}{c_C}+\frac{1}{c_D} \end{bmatrix}. \tag{33}$$

On substituting the equilibrium values of the components for a particular phase in Eq. 33, and inverting the resultant matrix, we get:

$$\frac{\partial c}{\partial \mu}^{s} = \begin{bmatrix} 0.000555 & -0.000013 & -0.000099 \\ -0.000013 & 0.023264 & -0.004229 \\ -0.000099 & -0.004229 & 0.145959 \end{bmatrix} \quad (34)$$

$$\frac{\partial c}{\partial \mu}^{l} = \begin{bmatrix} 0.00319 & -0.000029 & -0.00063 \\ -0.000029 & 0.009115 & -0.001811 \\ -0.00063 & -0.001811 & 0.15813 \end{bmatrix} \quad (35)$$

8.4. Phase-field simulation parameters

The values of the parameters controlling the interfacial energy and width in our phase-field simulations, are, $\sigma = 0.1$ and $\epsilon = 16$, respectively. A square grid with spacing $dx = dy = 4$, is used to discretize the dependent variable fields, and the time-stepping size is $dt = 0.25$. The simulation box was 2000 grid-points long, with its width being set by the perturbation wavelength considered.

8.5. Non-dimensionalization

In this study, all calculations are performed in a non-dimensionalized form. The non-dimensional numbers can be converted back to their dimensional forms for any system, using the following definitions of length, time and energy scales, determined by the dimensional values of the parameters for that particular system,

$$f^* = \frac{1}{V_m}\left[\frac{\partial \mu_i}{\partial c_j}\right]_{max}, \quad (36)$$

$$l^* = \frac{\sigma}{f^*}, \quad (37)$$

$$t^* = \frac{l^{*2}}{[D_{ij}]_{max}}. \quad (38)$$

In typical alloy solidification studies, $V_m = 10e{-}06\ m^3/mol$ and the maximum value of diffusivity ($[D_{ij}]_{max}$) is around $1e-09\ m^2/s$.

8.6. Tie-line and steady-state velocity selection during growth in a multicomponent alloy

The expressions which lead to the calculation of bulk liquid compositions (c_i^∞, i representing any of the $K-1$ independent solute elements in a K component alloy), each corresponding to a different scaling constant η_s ($= x_f/\sqrt{t}$, x_f being the position of the solidification front at time t) during steady-state solidification, for a given tie-line ($c_{i,eq}^l$) and independent solute diffusivities in the liquid (D_{ii}), are given as,

$$\{c_i^\infty\} = \left\{ c_{i,eq}^l - \frac{\sqrt{\pi}}{2} \frac{\eta_s \Delta c_i \operatorname{erfc}\left(\frac{\eta_s}{2\sqrt{D_{ii}}}\right)}{\sqrt{D_{ii}} \exp\left(\frac{-\eta_s^2}{4D_{ii}}\right)} \right\}, \quad (39)$$

where $\Delta c_i = c_{i,eq}^l - c_{i,eq}^s$, and $\{\cdot\}$ denotes a vector of length equal to the number of solutes in the alloy system.

We can also compute the equilibrium tie-line compositions ($c_{i,eq}^l$) and η_s from a knowledge of the bulk alloy compositions (c_i^∞) and the independent solute diffusivities in the liquid (D_{ii}), by solving a coupled set of non-linear equations given by,

$$\left\{\frac{-\sqrt{\pi}\eta_s \Delta c_i}{2\sqrt{D_{ii}}}\right\} = \left\{ \frac{(c_i^\infty - c_{i,eq}^l)}{\operatorname{erfc}\left(\frac{\eta_s}{2\sqrt{D_{ii}}}\right)} \exp\left(\frac{-\eta_s^2}{4D_{ii}}\right) \right\}, \quad (40)$$

where, we employ,

$$\left\{c_{i,eq}^{s,l}\right\} = \left\{c_{i,eq}^{s,l,*}\right\} + \left[\frac{\partial c_i^{s,l}}{\partial \mu_j}\right] \left\{\mu_{j,eq} - \mu_{j,eq}^*\right\}, \quad (41)$$

and,

$$\frac{1}{V_m}\left\{c_{i,eq}^{s,*} - c_{i,eq}^{l,*}\right\}\left\{\mu_{i,eq} - \mu_{i,eq}^*\right\} = 0. \quad (42)$$

to express $c_{i,eq}^{s,l}$ as functions of $\mu_{i,eq}$ (both Eqs. 41 and 42 are expressed in the matrix-vector notation with $[\cdot]$ denoting a matrix). In Eq. 41, $c_{i,eq}^{s,l,*}$ represents the compositions about which the phase diagram is linearized, with $\mu_{j,eq}^*$ representing the corresponding chemical potentials.

Eq. 42 is obtained from Eq. 28 under conditions of steady-state solidification by a planar front. Thus, for $K-1$ independent solutes, Eq. 40, represents same number of independent equations, with any of the $K-2$ (out of $K-1$) μ_i and η_s as the independent variables to be solved for. Once, they are known, the new equilibrium compositions $c_{i,eq}^{s,l}$ can be retrieved from Eq. 41 and Eq. 42.

References

[1] K. Fisher, W. Kurz, Fundamentals of solidification, Trans Tech Publications.

[2] W. W. Mullins, R. F. Sekerka, Stability of a planar interface during solidification of a dilute binary alloy, Journal of Applied Physics 35 (2).

[3] G. Ivantsov, Doklady Akad. Nauk. 58 (5) (1947) 567.

[4] G. Horvay, J. Cahn, Dendritic and spheroidal growth, Acta Metallurgica 9 (7) (1961) 695 – 705. doi:http://dx.doi.org/10.1016/0001-6160(61)90008-6.
URL http://www.sciencedirect.com/science/article/pii/0001616061900086

[5] J. Langer, H. Müller-Krumbhaar, Theory of dendritic growth—i. elements of a stability analysis, Acta Metallurgica 26 (11) (1978) 1681 – 1687. doi:http://dx.doi.org/10.1016/0001-6160(78)90078-0.
URL http://www.sciencedirect.com/science/article/pii/0001616078900780

[6] J. S. Langer, Instabilities and pattern formation in crystal growth, Rev. Mod. Phys. 52 (1980) 1–28. doi:10.1103/RevModPhys.52.1.
URL http://link.aps.org/doi/10.1103/RevModPhys.52.1

[7] J. Lipton, M. Glicksman, W. Kurz, Solidification microstructure: 30 years after constitutional supercooling dendritic growth into undercooled alloy metals, Materials Science and Engineering 65 (1) (1984) 57 – 63. doi:http://dx.doi.org/10.1016/0025-5416(84)90199-X.
URL http://www.sciencedirect.com/science/article/pii/002554168490199X

[8] W. Kurz, B. Giovanola, R. Trivedi, Theory of microstructural development during rapid solidification, Acta Metallurgica 34 (5) (1986) 823 – 830. doi:http://dx.doi.org/10.1016/0001-6160(86)90056-8.
URL http://www.sciencedirect.com/science/article/pii/0001616086900568

[9] J. Lipton, M. E. Glicksman, W. Kurz, Equiaxed dendrite growth in alloys at small supercooling, Metallurgical Transactions A 18 (2) 341–345. doi:10.1007/BF02825716.
URL http://dx.doi.org/10.1007/BF02825716

[10] J. Lipton, W. Kurz, R. Trivedi, Rapid dendrite growth in undercooled alloys, Acta Metallurgica 35 (4) (1987) 957 – 964. doi:http://dx.doi.org/10.1016/0001-6160(87)90174-X.
URL http://www.sciencedirect.com/science/article/pii/000161608790174X

[11] F. Weinberg, B. Chalmers, Dendritic growth in lead, Canadian Journal of Physics 29 (5) (1951) 382–392. arXiv:http://dx.doi.org/10.1139/p51-042, doi:10.1139/p51-042.
URL http://dx.doi.org/10.1139/p51-042

[12] F. Weinberg, B. Chalmers, Further observations on dendritic growth in metals, Canadian Journal of Physics 30 (5) (1952) 488–502. arXiv:http://dx.doi.org/10.1139/p52-047, doi:10.1139/p52-047.
URL http://dx.doi.org/10.1139/p52-047

[13] C. S. Lindenmeyer, B. Chalmers, Growth rate of ice dendrites in aqueous solutions, The Journal of Chemical Physics 45 (8).

[14] M. E. Glicksman, R. J. Schaefer, J. D. Ayers, Dendritic growth-a test of theory, Metallurgical Transactions A 7 (11) (1976) 1747–1759. doi:10.1007/BF03186673.
URL http://dx.doi.org/10.1007/BF03186673

[15] K. Somboonsuk, R. Trivedi, Dynamical studies of dendritic growth, Acta Metallurgica 33 (6) (1985) 1051 – 1060. doi:http://dx.doi.org/10.1016/0001-6160(85)90198-1.
URL http://www.sciencedirect.com/science/article/pii/0001616085901981

[16] C. B. Arnold, M. J. Aziz, M. Schwarz, D. M. Herlach, Parameter-free test of alloy dendrite-growth theory, Phys. Rev. B 59 (1999) 334–343. doi:10.1103/PhysRevB.59.334.
URL http://link.aps.org/doi/10.1103/PhysRevB.59.334

[17] S. Akamatsu, G. Faivre, T. Ihle, Symmetry-broken double fingers and seaweed patterns in thin-film directional solidification of a nonfaceted cubic crystal, Phys. Rev. E 51 (1995) 4751–4773. doi:10.1103/PhysRevE.51.4751.
URL http://link.aps.org/doi/10.1103/PhysRevE.51.4751

[18] S. Akamatsu, H. Nguyen-Thi, In situ observation of solidification patterns in diffusive conditions, Acta Materialia 108 (2016) 325 – 346. doi:http://dx.doi.org/10.1016/j.actamat.2016.01.024.
URL http://www.sciencedirect.com/science/article/pii/S1359645416300234

[19] C. W. Lan, C. J. Shih, Efficient phase field simulation of a binary dendritic growth in a forced flow, Phys. Rev. E 69 (2004) 031601. doi:10.1103/PhysRevE.69.031601.
URL http://link.aps.org/doi/10.1103/PhysRevE.69.031601

[20] J. C. Ramirez, C. Beckermann, A. Karma, H.-J. Diepers, Phase-field modeling of binary alloy solidification with coupled heat

and solute diffusion, Phys. Rev. E 69 (2004) 051607. doi:10.1103/PhysRevE.69.051607.
URL http://link.aps.org/doi/10.1103/PhysRevE.69.051607

[21] J. Ramirez, C. Beckermann, Examination of binary alloy free dendritic growth theories with a phase-field model, Acta Materialia 53 (6) (2005) 1721 – 1736. doi:http://dx.doi.org/10.1016/j.actamat.2004.12.021.
URL http://www.sciencedirect.com/science/article/pii/S135964540400758X

[22] B. Böttger, J. Eiken, M. Apel, Phase-field simulation of microstructure formation in technical castings – a self-consistent homoenthalpic approach to the micro–macro problem, Journal of Computational Physics 228 (18) (2009) 6784 – 6795. doi:http://dx.doi.org/10.1016/j.jcp.2009.06.028.
URL http://www.sciencedirect.com/science/article/pii/S0021999109003210

[23] S. Gurevich, A. Karma, M. Plapp, R. Trivedi, Phase-field study of three-dimensional steady-state growth shapes in directional solidification, Phys. Rev. E 81 (2010) 011603. doi:10.1103/PhysRevE.81.011603.
URL http://link.aps.org/doi/10.1103/PhysRevE.81.011603

[24] Y. Ma, M. Plapp, Phase-field simulations and geometrical characterization of cellular solidification fronts, Journal of Crystal Growth 385 (2014) 140 – 147, the 7th International Workshop on Modeling in Crystal Growth. doi:http://dx.doi.org/10.1016/j.jcrysgro.2013.03.027.
URL http://www.sciencedirect.com/science/article/pii/S0022024813002145

[25] B. Echebarria, R. Folch, A. Karma, M. Plapp, Quantitative phase-field model of alloy solidification, Phys. Rev. E 70 (2004) 061604. doi:10.1103/PhysRevE.70.061604.
URL http://link.aps.org/doi/10.1103/PhysRevE.70.061604

[26] D. Coates, S. Subramanian, G. Purdy, Solid-liquid interface stability during solidification of dilute ternary alloys, TRANS MET SOC AIME 242 (5) (1968) 800–809.

[27] S. Coriell, G. McFadden, P. Voorhees, R. Sekerka, Stability of a planar interface during solidification of a multicomponent system, Journal of Crystal Growth 82 (3) (1987) 295 – 302. doi:http://dx.doi.org/10.1016/0022-0248(87)90317-4.
URL http://www.sciencedirect.com/science/article/pii/0022024887903174

[28] O. Hunziker, Theory of plane front and dendritic growth in multicomponent alloys, Acta Materialia 49 (20) (2001) 4191 – 4203. doi:http://dx.doi.org/10.1016/S1359-6454(01)00313-5.
URL http://www.sciencedirect.com/science/article/pii/S1359645401003135

[29] A. Choudhury, B. Nestler, Phys.Rev.E 85 (2011) 021602.

[30] A. Choudhury, Quantitative phase-field model for phase transformations in multi-component alloys, Vol. Band 21, KIT Scientific Publishing, 2012.

[31] A. Lahiri, T. A. Abinandanan, A. Choudhury, M. S. Bhaskar, Theoretical and numerical determination of phase concentrations during growth in ternary alloysdoi:arXiv:1602.05341.
URL http://arxiv.org/abs/1602.05341